Observation of an intermediate phase in tungsten doped Sb_2Te phase change thin films by temperature dependent measurements of structural, optical, and electronic properties

2016 J. Phys. D: Appl. Phys. 49 265105

(http://iopscience.iop.org/0022-3727/49/26/265105)

IOP Publishing Journal of Physics D: Applied Physics
J. Phys. D: Appl. Phys. **49** (2016) 265105 (9pp) doi:10.1088/0022-3727/49/26/265105

Observation of an intermediate phase in tungsten doped Sb_2Te phase change thin films by temperature dependent measurements of structural, optical, and electronic properties

S Guo[1], T Huang[1], L P Xu[1], K Shi[1], J Z Zhang[1], X L Ji[2], Z G Hu[1], L C Wu[2], Z T Song[2] and J H Chu[1]

[1] Department of Electronic Engineering, East China Normal University, Shanghai 200241, People's Republic of China
[2] State Key Laboratory of Functional Materials for Informatics, Shanghai Institute of Microsystem and Information Technology, Chinese Academy of Sciences, Shanghai 200050, People's Republic of China

E-mail: zghu@ee.ecnu.edu.cn

Received 19 March 2016
Accepted for publication 8 April 2016
Published 25 May 2016

Abstract

The optical properties, electronic structure, and microstructure of Sb_2Te (ST) phase change films as functions of temperature and tungsten (W) concentration have been investigated by means of temperature dependent x-ray diffraction (XRD), Raman scattering, and spectroscopic ellipsometry. Based on the variations of the diffraction peaks, phonon modes, and dielectric functions during the temperature elevation process, the intermediate (INT) crystalline state of W doped Sb_2Te (WST) films between amorphous (AM) and hexagonal (HEX) phases can be readily proposed, which is a mixture of crystalline Sb and Te. The anomalous behaviors of dielectric functions and partial spectral weight integral for crystalline films elucidate the existence of INT state. Furthermore, the good agreement between experimental and calculated dielectric functions reveals that the first-principles calculation method can be used to make qualitative analysis in the materials with similar multilayered structures.

Keywords: phase change films, optical properties, doped-Sb_2Te, Raman scattering, spectroscopic ellipsometry

S Online supplementary data available from stacks.iop.org/JPhysD/49/265105/mmedia

(Some figures may appear in colour only in the online journal)

1. Introduction

Chalcogenide alloys have been extensively investigated for information storage based on the fast and reversible change between amorphous (*a*-) and crystalline (*c*-) phases, induced by an electric pulse [1, 2]. The ternary alloy $Ge_2Sb_2Te_5$ (GST) is one of the most widely used for data storage due to its good trade-off between crystallization speed and amorphous thermal stability [3]. However, the nucleation-dominated crystallization mechanism of GST imposes restrictions on the crystallization rate. Compared with GST, the δ-phase Sb_2Te (ST) alloy exhibits a growth-dominated crystallization behavior, low melting point, and large amorphous/crystalline resistance ratio. The characteristics can be beneficial to generate a higher operation speed and lower power consumption for memory devices [4]. Therefore, Sb_2Te shows the potential to be a promising candidate of GST for incumbent storage mediums [4, 5].

In previous study, crystalline Sb-rich Sb–Te compounds with a Sb concentration above 40% are composed of Sb_2Te_3 units and Sb bilayers [6]. The formation of Sb_2 can help to speed up the crystallization for amorphous films, which can increase the crystallization rate of phase change materials. Similar with other Sb–Te system materials, Sb_2Te has the relatively lower crystallization temperature, which leads to the lower thermal stability [5]. The problems have been solved by effectively tungsten (W) doping [7], which shows the better performance compared with other dopants, such as N [8], Si [9], Al [10], and Cu [11]. Compared with these dopants, Sb_2Te is very susceptible to W doping. A thimbleful of W can change the performance of ST greatly, which can minimise the phase separation. The W atom radius is 139 pm, which is similar to that of Te (140 pm) and Sb (145 pm). Most of the W atoms act as substitutional impurities in the crystal lattice of ST, which can be confirmed by transmission electron microscopy (TEM) images and the corresponding selected area electron diffraction (SAED) of W doped Sb_2Te (WST) films. The ST and WST films show the final crystalline phase with a hexagonal (HEX) lattice ($P-3m1$) [7].

In the present work, the intermediate (INT) state of WST films between amorphous (AM) and HEX phases can be confirmed with the aid of temperature dependent XRD, Raman scattering, and spectroscopic ellipsometry (SE) experiments. The complex crystallization mechanism and dielectric functions have been discussed in detail. Finally, the comparison between experimental and calculated dielectric functions of ST in HEX phase has been presented.

2. Experimental details

2.1. Structural and optical characterizations

The ST and WST films were deposited on SiO_2/Si (1 0 0) substrates at room temperature via cosputtering pure stoichiometric Sb_2Te and W targets with a thickness of about 220 nm. The background and Ar gas pressure of the sputtering system were set to 1.8×10^{-4} and 0.21 Pa, respectively. Energy dispersive spectrometer (EDS) confirms that the W concentration is around 3.2, 5.4, and 7.8% in the WST films (named WST3.2%, WST5.4%, and WST7.8%, respectively). The structure variations of ST film were investigated by temperature dependent XRD at a fixed heating rate of 10 K min^{-1} in the temperature range from 300 to 600 K under vacuum condition (D8 Advance, Bruker). Raman spectra have been collected on heating by a Jobin-Yvon LabRAM HR 800 micro-Raman spectrometer with a resolution better than 1 cm^{-1} and a THMSE 600 heating/cooling stage (Linkam Scientific Instruments) at a fixed heating rate of 10 K min^{-1} in the temperature range from 210 to 620 K. The Ar^+ laser with the wavelength of 488 nm at a power of 5 mW was taken as the exciting source. The laser beam was focused through a 50 × microscope with a working distance of 18 mm. An air-cooled charge coupled device (CCD) (−70 °C) with a 1024 × 256 pixels front illuminated chip was utilized to collect the scattered signal dispersed on 1800 grooves mm^{-1} grating. The temperature dependent SE measurements were performed in the photon energy range of 0.1–4.13 eV (300–12 400 nm) at an incident angle of 70° by a vertical variable-angle SE (J. A. Woollam Co., Inc.). The spectral resolution was set to 5 nm and the measurements were carried out with auto retarder (high accuracy). The samples were mounted into an Instec cell and Janis CRV-217V with liquid nitrogen as cooling accessories for high and low temperature experiments, respectively. The temperature is varied from 210 to 620 K with a precision of about ±1 K. Note that the window corrections were included as a part of the model during the fitting analysis.

2.2. Theoretical approach

Computations were performed at the East China Normal University computing center. The plane-wave-based density functional theory (DFT) calculation with the generalized gradient approximation (GGA) of Perdew–Burke–Ernzerhof (PBE) was carried out for Sb_2Te to obtain the information about the energy structure [12]. In order to account for the effect of London dispersion forces, we use the van der Waals density functional (vdW-DF) as implemented in the VASP code [13]. In particular, we have used the so-called optB86b-vdW functional, which provides superior values for the lattice constants in comparison with other vdW-DF functionals. For total-energy calculations and the optimization of the structures we used a standard plane-wave basis set with a kinetic-energy cutoff value of 800 eV. For the Brillouin-zone integration we used a 16 × 16 × 3 grid [14]. The convergence criterion for the electronic energy is 10^{-6} eV. The electronic structures and optical properties are calculated with the corresponding optimized crystal geometries. Optical properties of a material can be measured from the complex dielectric function, which consists of a real part ε_1 and an imaginary part ε_2.

3. Results and discussion

3.1. X-ray diffraction

The crystal structure variations of ST film during the complex crystallization process with increasing temperature have been revealed by *in situ* XRD, as shown in figure 1. No diffraction peaks appear in ST film at room temperature (300 K), suggesting that the as-deposited film is of amorphous state. Note that the bump around 30 degree in the XRD spectrum at 300 K is an inherent characteristic of Ge-Sb–Te systems in amorphous structure. As the temperature rising to 390 K, diffraction peaks of crystalline Sb and Te start to appear, namely, the first phase change temperature (T_{c1}) is about 390 K. It shows that the *a*-ST film crystallizes into the mixture of Sb and Te crystals. The increasing intensity of diffraction peaks upon heating can be attributed to the increment of crystalline Sb and Te. With further heating up, it is interesting to find that several new diffraction peaks belonging to hexagonal crystalline phase of ST film occur at about 540 K, which corresponds to the second phase change temperature (T_{c2}). The diffraction peaks for hexagonal ST are marked as (0 0 4), (0 0 5), (1 0 3), (0 1 6), (1 1 0), (1 1 4), and (0 2 3), respectively

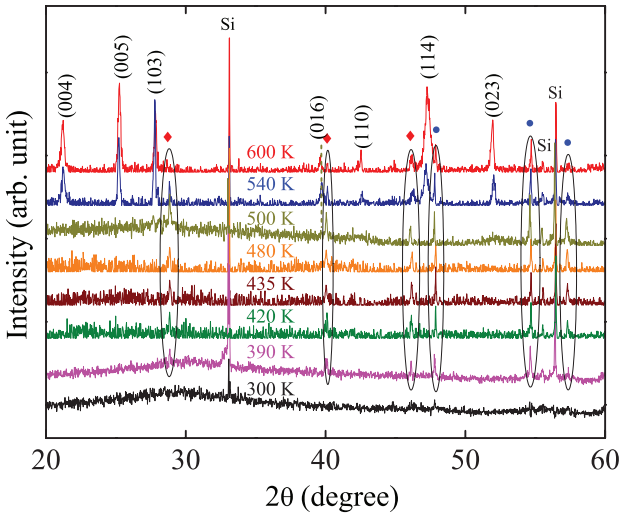

Figure 1. Temperature dependent XRD patterns of ST film at several characteristic temperatures. The red diamonds and blue dots indicate the diffraction peaks of crystalline Sb and Te, respectively.

[15]. Furthermore, with increasing temperature, the intensity of the hexagonal ST peaks exhibits an increasing trend gradually and the strength of crystalline Sb and Te peaks becomes weaken slowly. The situation should be associated with the decrease of crystalline Sb and Te during the formation of HEX ST. Moreover, no other diffraction peak in *c*-ST film can be observed. It can be concluded that there is an intermediate state during the phase change from amorphous to HEX phase for ST film, which contains crystalline Sb and Te. Note that the phenomenon was not discovered in previous studies due to the rapid crystalline process induced by rapid thermal annealing or an electrical impulse [7–9].

3.2. Raman scattering

The nondestructive Raman scattering has been widely used to investigate the phase change in chalcogenide alloys, which provides precise information about local distortions and ionic configurations in the crystal structures [16–20]. To further analyze the process of crystallization and the W doping effects, temperature dependent Raman scattering experiment was performed. Figure 2 displays Raman spectra of ST and WST films recorded at several characteristic temperatures. The main feature of Raman spectra for amorphous ST and WST films is a broadening band covering from 60 to 180 cm^{-1} frequency region. The Raman spectra of ST film exhibit two significant variations with increasing temperature (figure 2(a)). Note that the structure variations of ST film and the two corresponding transition temperatures, namely T_{c1} and T_{c2}, are in accordance with the result from temperature dependent XRD, as shown in figure 1. The similar phase change behaviors are exhibited in WST3.2% and WST5.4% films depicted in figures 2(b) and (c), respectively. It is noteworthy that only the transition from AM to INT state can be discovered for WST7.8% film until the temperature rising to 620 K (figure 2(d)). The parameter T_{c1} can be estimated to 390, 420, 460, and 500 K for ST, WST3.2%, WST5.4%, and WST7.8% films, respectively. Meanwhile, the parameter T_{c2} for ST, WST3.2%, and WST5.4% films can be, in order, about 530, 550, and 580 K, respectively. It can be concluded that the W introduction shows an inhibition on the crystallization behavior. Note that the two peaks located at about 189 and 254 cm^{-1} are corresponding to the Sb-O-Sb stretching (A_1 type) and bending (T_2 type) vibrational modes of Sb_2O_3, respectively [21]. The oxidization at higher temperatures is due to the existence of a small amount of oxygen under the condition of nitrogen. The temperature of the appearance for Sb_2O_3 peaks is elevated from 530 to 570 K with the W concentration increasing to 5.4%. The two Raman peaks from Sb_2O_3 cannot be observed for WST7.8% film in the present experimental temperature range. It indicates that W dopants can suppress oxidization of Sb_2Te film during the process of heating up. Note that the HEX phase mentioned in this study was not those of pure HEX Sb_2Te, but those of mixed state with HEX state and a small amount of INT state (crystalline Sb and Te).

To provide an in-depth analysis of the crystallization mechanism (AM-INT and INT-HEX phase changes) and the W doping effects on ST film, Raman spectra for ST and WST films were fitted with the aid of Lorentz–Gauss oscillator model to describe the vibrational modes. Raman spectra of ST and WST films at three typical temperatures (300, 500, and 600 K) and the well-fitted deconvolution peaks for ST film are depicted in figure 3. For *a*-Sb_2Te structure, all the atoms are in a defective octahedral environment. The majority of primitive rings are four- or five-membered. The Raman spectra of *a*-ST are derived from heteropolar Sb–Te and homopolar Sb–Sb bond vibrations, as shown in figure 3(a). Note that few Te–Te bonds exist in *a*-ST [22]. The eutectic composition Sb_2Te ultimately crystallizes into trigonal structure with hexagonal unit cell containing nine layers stacked along the *c* axis, which presents the combination of five-layer stacks of Sb_2Te_3 and two-layer stacks of Sb_2 [23]. The bonding between Sb_2Te_3 units and Sb bilayers, as well as between adjacent Sb bilayers, is of the van der Waals type [6]. The Raman peaks of ST are marked with Arabic numerals from 1 to 8 for INT state (500 K) and HEX phase (600 K), as shown in figures 3(b) and (c), respectively. The frequencies of phonon modes for ST and WST films are listed in table S1 (supplementary data (stacks.iop.org/JPhysD/49/265105/mmedia)). Peak 1 (69 cm^{-1}) is the A_{1g} (1) mode for Sb–Te bond vibrations [24]. Peaks 2, 4, and 5 are the Te peaks, which can be assigned to E_{1g}, A_{1g}, and E_{2g} vibrational modes at about 90 cm^{-1}, 122 cm^{-1}, and 141 cm^{-1}, respectively [25, 26]. The derivations of the four Raman phonon modes mentioned above are consistent in INT and HEX structures. Peak 3 (102 cm^{-1}) and 6 (155 cm^{-1}) are corresponding to E_g and A_{1g} phonon modes of Sb–Sb bonds for crystalline Sb in INT state [27, 28]. Therefore, it can be summarized that the INT state is consist of crystalline Sb and Te for ST film. Peaks 3 and 6 in HEX phase come from two geometries, namely crystalline Sb and Sb bilayers in HEX ST. Peak 7 (111 cm^{-1}) and 8 (163 cm^{-1}) emerge gradually with further increasing temperature in HEX phase, which correspond to $E_g(2)$ and $A_{1g}(2)$ vibrational modes for Sb–Te bonds in Sb_2Te_3 units, respectively [24].

In addition, a sharp decrease of relative strength ratio of peak 4 and 6 (namely the strength of 4/6 ratio) can be observed

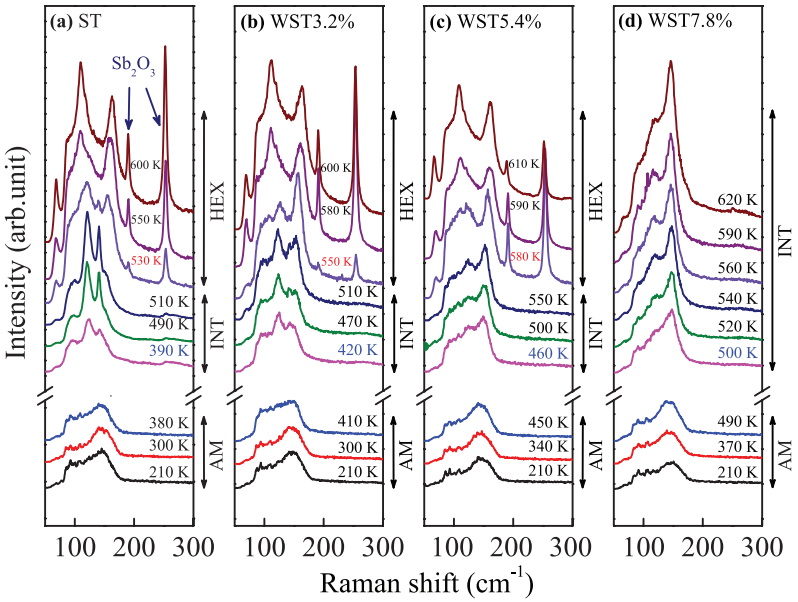

Figure 2. Temperature dependent Raman spectra from 210 to 620 K. (a) ST, (b) WST3.2%, (c) WST5.4%, and (d) WST7.8%. Note that the two peaks located at about 189 cm^{-1} and 254 cm^{-1} correspond to the oxide phase of Sb_2O_3.

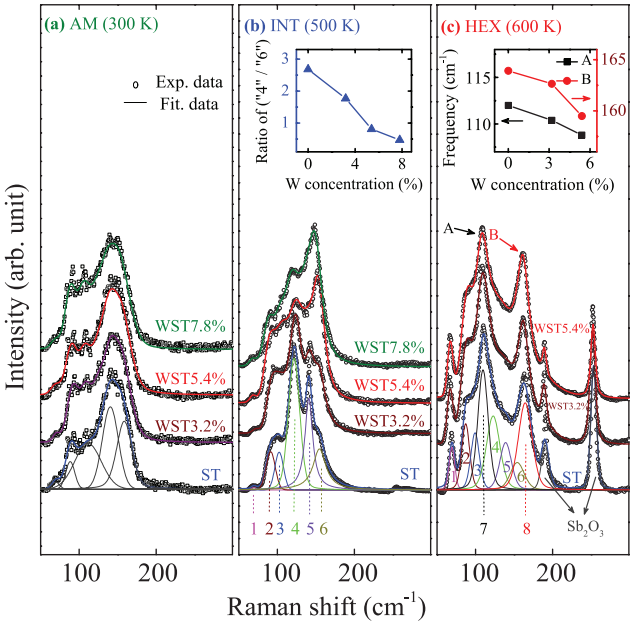

Figure 3. Raman spectra of (a) *a*-WST at 300 K and *c*-WST at (b) 500 K and (c) 600 K with different W concentration, respectively. Note that the fitting to the Lorentz–Gaussian functions for *a*-ST and *c*-ST is given as an example. The insets of (b) and (c) show the relative strength ratio evolution of peak 4 and 6, and the frequency variations of the two main peaks (A and B) as a function of W concentration, respectively.

with increasing the W concentration, as shown in the inset of figure 3(b). For comparison, the W doping can inhibit the formation of Te–Te bonds and promote the bonding of Sb atoms. The two main Raman peaks (A and B) in HEX phase shift to a lower wave numbers with increasing W concentration (the inset of figure 3(c)). The frequency redshift should be attributed to the substitution of Te and/or Sb by W atoms [7]. The relative strength of peak 1 increases sharply in the HEX geometry as compared with INT state. However, that of peak 4 and 5 decreases. Due to the fact that there is few Sb_2Te_3 units in INT state, the number of Te–Te bonds decreases relatively in HEX phase. Note that a small amount of Sb–Sb and Te–Te bonds of crystalline Sb and Te still exist in the final HEX geometry, which can be attributed to the incomplete recrystallization caused by the slow heating rate [16]. Nevertheless, it must be stressed that the incomplete recrystallization phenomena do not appear in the corresponding memory devices induced by an electrical impulse.

Figure 4 shows the phonon frequency evolutions as a function of temperature for ST and WST films. Phase changes from AM to INT state and then to HEX phase can be identified easily. It can be seen that both T_{c1} and T_{c2} have a shift towards higher temperature. Raman spectra change from a broadening band to a series of overlapping peaks coming from crystalline Sb and Te at about T_{c1}. The phase change from AM to INT state can be described as the breaking of primitive multi-membered rings containing Sb–Sb and Sb–Te bonds, as well as the formation of Sb–Sb and Te–Te bonds (namely a mixture of crystalline Sb and Te). The crystallization process leads to a dramatic order degree increment. Peak 7 and 8 appear gradually when the temperature approaches to about T_{c2}. The structure variation from INT state to HEX phase corresponds to the breaking of Sb–Sb and Te–Te bonds, as well as the formation of Sb–Te bonds. The break of Te–Te bonds is in coincidence with the relative strength decrease of peak 4 and 5 during the change from INT state to HEX phase as discussed in figure 3. In addition, the frequencies of peak 3 and 6 decrease slightly during the transition from INT state to HEX phase. The phenomenon can be associated with the formation of Sb–Sb bonds in layered HEX structure. The HEX phase cannot be observed in WST7.8% film in the range of experimental temperature (below 620 K). Therefore, the detailed crystallization mechanism of ST film as the function of temperature can be describe as: With increasing temperature, amorphous alloy crystalizes into crystalline Sb and Te mixture at about

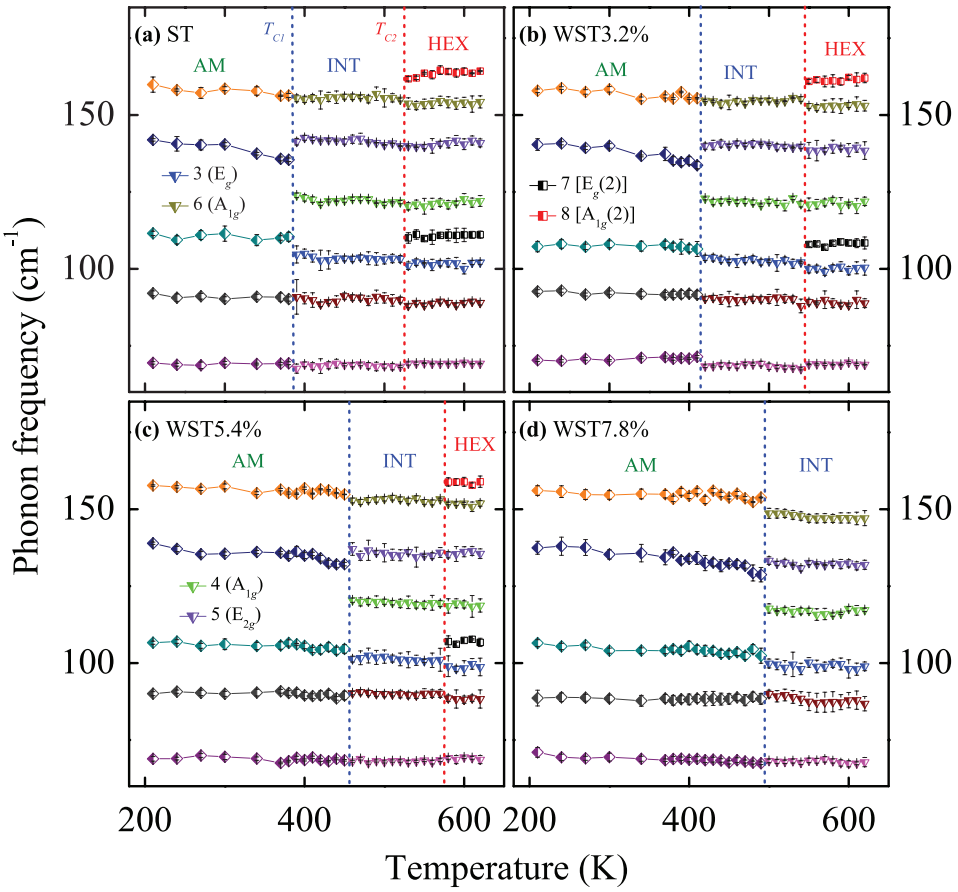

Figure 4. Phonon frequency evolutions as a function of temperature for ST and WST films. Note that the dotted lines show the respective phase change temperatures.

T_{c1}, namely, the intermediate state. With further heating, the mixed crystal recrystallizes into the HEX phase.

3.3. Spectroscopic ellipsometry

The optical behaviors of the ST and WST films with different crystal structures were investigated by temperature dependent SE based on the reflectance configuration. It is a sensitive optical method to characterize thin films and surfaces, which measures the relative changes in amplitude and phase of polarized lights upon oblique reflection from sample surface [29]. The experimental data measured by ellipsometry are the ratio p in terms of Ψ and Δ, defined as $p = r_p/r_s = \tan\Psi e^{i\Delta}$, here, r_p and r_s are the reflection coefficient of the polarized lights parallel and perpendicular to the incidence plane angle, respectively. The ratio p is the function of photon energy, incident angle, and dielectric functions (ε) of the materials. The complex dielectric functions can be calculated directly for the material with idealized surface: $\varepsilon = \varepsilon_1 + i\varepsilon_2 = \sin^2\theta[1 + \tan^2\theta(1-p)^2/(1+p)^2]$; here, θ is the incident angle [30]. Note that the imaginary part can reflect the electronic transition information of the films. To extract the dielectric functions of WST films, the ellipsometric spectra were evaluated by a five-layered model (air/surface rough layer/WST/SiO_2/Si). The fitting procedure was carried out with WVASE32 software package (J. A. Woollam Co., Inc.). The surface rough layer was defined by effective medium approximation with a mixture of film (50%) and void (50%). The dielectric functions were obtained by Tauc–Lorentz (TL) and Lorentz dispersion models for amorphous and crystalline films, respectively. The TL model has been widely applied in semiconductors or dielectric materials successfully [29, 31, 32]. The imaginary part of TL model can be written as [33, 34]:

$$\varepsilon_2 = \begin{cases} \dfrac{AE_nC(E-E_g)^2}{(E^2-E_n^2)^2 + C^2E^2}\dfrac{1}{E} & (E > E_g) \\ 0 & (E \leqslant E_g) \end{cases} \quad (1)$$

and the real part is given by the Kramers–Krönig transformation (KKT)

$$\varepsilon_1 = \varepsilon_\infty + \frac{2}{\pi}P\int_{E_g}^{\infty}\frac{\xi\varepsilon_2(\xi)}{\xi^2 - E^2}\mathrm{d}\xi. \quad (2)$$

Here, A, E_n, C, and E_g is amplitude, peak transition energy, broadening term, and Tauc gap energy of the oscillator, respectively. P is the Cauchy principal part of the integral, ε_∞ is the high frequency dielectric constant, and E is the incident photon energy. The Lorentz model can be written as:

$$\varepsilon = \varepsilon_\infty + \sum_{k=1}^{n}\frac{A_k{E_k}^2}{{E_k}^2 - E^2 - iEC_k}. \quad (3)$$

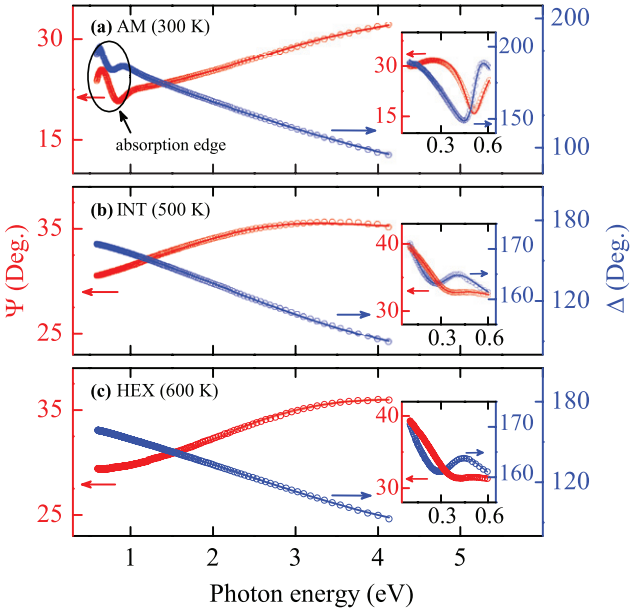

Figure 5. Experimental (dots) and best fitting (solid lines) ellipsometric spectra of Ψ and Δ of ST film for (a) AM (300 K), (b) INT (500 K), and (c) HEX (600 K) structures in UV-vis region of 0.6–4.13 eV, respectively. Note that the insets show the corresponding Ψ and Δ in the IR region of 0.1–0.6 eV.

Here, A_k, E_k, and C_k denotes the strength, center energy, and broadening term of the k_{th} oscillator, respectively. A Drude-like term for free carriers was added in ultraviolet (UV)-visible (vis) region of 0.6–4.13 eV for crystalline films and infrared (IR) region of 0.1–0.6 eV for amorphous and crystalline films [35–37]. The Drude model can be written as:

$$\varepsilon = -\frac{A_d B r_d}{E^2 + \mathrm{i} B r_d E}. \tag{4}$$

Here A_d and Br_d are the amplitude and broadening term of the oscillator, respectively. Figure 5 shows the experimental and best fitting ellipsometric spectra Ψ and Δ of ST film for AM (300 K), INT (500 K), and HEX (600 K) structures. The absorption edge, namely the band-edge of optical absorption, shows an obvious redshift from amorphous to crystalline phase. The dielectric functions of the ST and WST films can be extracted by fitting the model function to the measured data. The best fitting parameters for the films at 300 K (AM), 500 K (INT), and 600 K (HEX) are given in table S2 (supplementary data).

It is known that the dielectric functions are essentially associated with the energy band structure. The structure variations could lead to the obvious distinctions of optical constants during the phase change process. Evolutions of the imaginary part (ε_2) for ST and WST7.8% films at several typical temperatures extracted from ellipsometric measurements are shown in figures 6(a)–(d), respectively. The broad peaks for ε_2 of ST for AM, INT, and HEX geometries are around 2.0, 1.2, and 1.5 eV, respectively. For ST and WST films, the narrowing, redshift, and large enhancement of the main peak for ε_2 from amorphous to crystalline structure can be observed in UV-vis region of 0.6–4.13 eV (figures 6(b) and (d)). Furthermore, an obvious enhancement of Drude peaks in IR region of

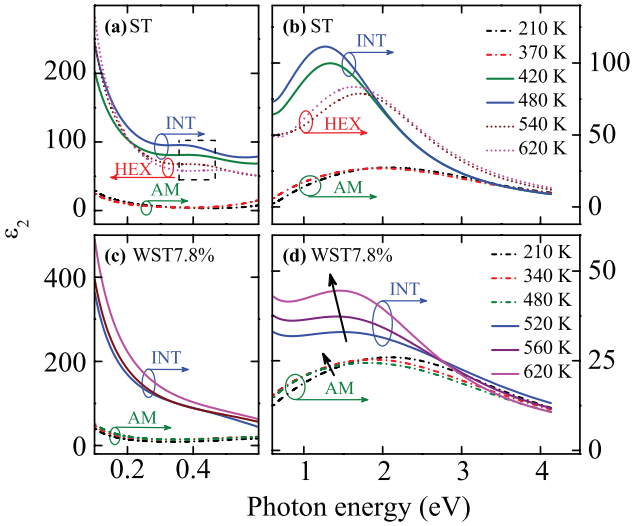

Figure 6. Evolutions of the imaginary part (ε_2) of ST and WST7.8% films at several typical temperatures. (a) and (c) IR region of 0.1–0.6 eV and (b) and (d) UV-vis region of 0.6–4.13 eV.

0.1–0.6 eV for crystalline structures can be found (figures 6(a) and (c)). The enormous difference of dielectric functions between amorphous and crystalline structures should be due to the order degree increment of after crystallization. That is to say, the significant optical contrast can be attributed to the variations of structure and chemical bonding [32, 35]. It is well known that the gradual evolutions of dielectric functions with increasing temperature are mainly associated with the electron–phonon interaction and lattice thermal expansion [38]. The overall vertical shifts of dielectric functions, namely, a redshift with elevated temperature, are from the temperature effects, as shown in figures 6(b) and (d). For crystalline ST, the ε_2 shifts to a lower energy gradually with increasing temperature. Then it shows an obvious blueshift abruptly at about 520 K (T_{c2}). The abnormal behavior can be attributed to the transition from INT to HEX state for ST film based on the results of temperature dependent XRD and Raman scattering experiments. It also can be summarized by the enhanced Drude peaks for HEX phase compared with INT state in IR region. The similar phase change behavior can be found in WST3.2% and WST5.4% films. However, for crystalline WST7.8%, the ε_2 shifts to the lower energy monotonically. It indicates that only the change from AM to INT structure can be occurred in WST7.8% film until the temperature approaching to 620 K, which is in accordance with the results of temperature dependent Raman scattering.

It is a remarkable fact that a small broad peak for ε_2 of ST film in INT and HEX geometries can be observed at about 0.37 and 0.4 eV, respectively (see the rectangle boxes in figure 6(a)). The peaks for ε_2 correspond to electronic transitions between the valence and conduction bands or other intraband transitions. The weak transition in IR region (0.1–0.6 eV) originates from two possible aspects: one is the band-to-band electronic transition due to the band gap narrowing during the change from amorphous to crystalline state, the other is the new intraband electronic transition ascribed to the high temperature. The abnormal behavior of

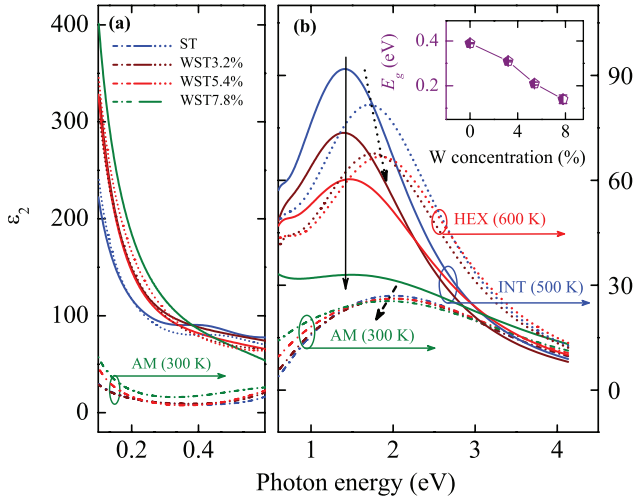

Figure 7. Evolutions of the imaginary part (ε_2) of ST and WST films for AM (300 K), INT (500 K), and HEX (600 K) structures with different W concentration. (a) IR region of 0.1–0.6 eV and (b) UV-vis region of 0.6–4.13 eV. Note that the inset of (b) shows the Tauc gap energy (E_g) for amorphous films as a function of W concentration determined from the simulation of ellipsometric spectra by Tauc–Lorentz model.

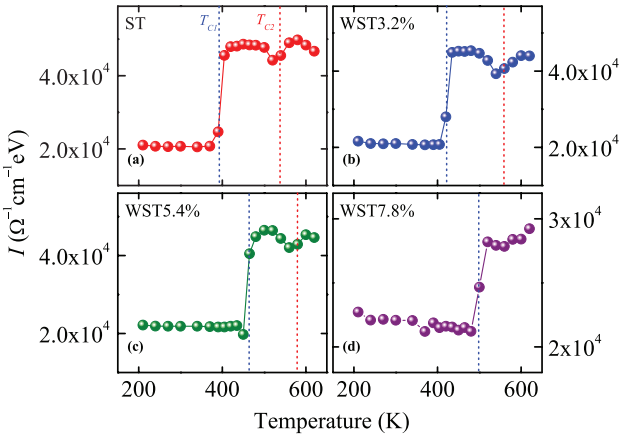

Figure 8. Partial spectral weight integral (I) evolutions of the ST and WST films in the photon energy region of 0.1–4.13 eV. (a) ST, (b) WST3.2%, (c) WST5.4%, and (d) WST7.8% as a function of temperature. Note that the dotted lines show the respective phase change temperatures.

ε_2 for crystalline film in IR region, namely, the blueshift with increasing temperature, can be associated with the change from INT to HEX geometry. The phenomenon is corresponding to the blueshift of ε_2 in UV-vis region, as shown in figure 6(b). Nevertheless, the additional electronic transition in low energy region cannot be discovered in WST films.

To analyze the W doping effects on dielectric functions, the evolutions of ε_2 for ST and WST films in AM (300 K), INT (500 K), and HEX (600 K) structures with different W concentration are shown in figure 7. The opposite variation trend of the ε_2 peaks in AM and HEX phases for ST and WST films can be discovered in UV-vis region (figure 7(b)). The peaks show a redshift with increasing W concentration for amorphous films, which can be attributed to the decreased interband transition energy by W doping. The majority of W atoms enters into the crystal lattice during the formation of HEX geometry, which can be regarded as substitutional impurities. Therefore, the W dopants lead to a disorder of HEX phase [7]. The disorder effect can be improved with increasing W concentration, which leads to a blueshift of ε_2 for HEX films. However, the vertical position of the peaks is nearly invariable for intermediate structure, which can be concluded that the effect on order degree of mixture crystals (Sb and Te) by W doping is insignificant. Note that the INT-HEX transition cannot be summarized from the dielectric function for WST7.8% film. The inset of figure 7(b) shows the Tauc gap energy (E_g) for amorphous films as a function of W concentration extracted from the Tauc–Lorentz model. It can be concluded that the parameter E_g is monotonously decreased with increasing W concentration. The band gap narrowing for W doped ST can be ascribed to the metallicity enhancement compared with undoped ST, which could be used to explain the disappeared low-energy transition of WST films in IR region at about 0.4 eV [32].

To further confirm the existence of intermediate state of ST and WST films during the transition from AM to HEX phase, the partial spectral weight integral (I) evolutions in the photon energy region of 0.1–4.13 eV are shown in figure 8. The parameter I can reflect the electrons excited by photons in the selected energy range. It is defined as [39]:

$$I = \int_{E_1}^{E_2} \sigma_1(E)\mathrm{d}E, [\sigma_1(E) = \varepsilon_0\varepsilon_2(E)E]. \quad (5)$$

Here, $\sigma_1(E)$ is the optical conductivity, E_2 and E_1 are the upper and lower bound of the energy range, respectively. The parameter I of all four films decreases slightly in the initial heating stage with increasing temperature, which can be attributed to the thermal activation leading electronic transition as a function of temperature. The I near T_{c1} increases sharply, which is corresponding to the phase change from AM to INT structure. It can be associated with the strong absorption during the crystallization process. With further increasing temperature, the partial spectral weight integral decreases to a minimum value, then it continues to increase. The temperature discontinuities can be associated with the transition from INT to HEX phase for ST and WST films, which is corresponding to the T_{c2}. For WST7.8% film, the temperature discontinuity could not be found in the experimental temperature range (below 620 K). The parameter T_{c1} can be estimated to 390 K, 420 K, 465 K, and 500 K for ST, WST3.2%, WST5.4%, and WST7.8% films, respectively. The parameter T_{c2} for ST, WST3.2%, and WST5.4% films could be, in order, about 540 K, 560 K, and 580 K. The inhibition on the crystallization behavior by W introduction, as well as the two corresponding transition temperatures, namely T_{c1} and T_{c2}, are in good agreement with the results from temperature dependent XRD and Raman scattering experiments.

3.4. Density functional theory calculations

The crystalline structure of Sb_2Te in HEX geometry is depicted in figure 9(c), which is a nine layers stacked along

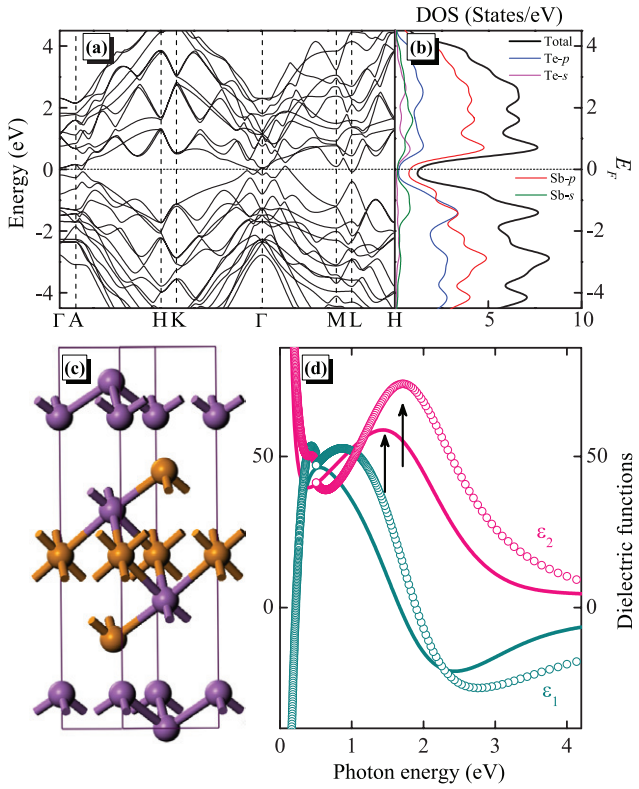

Figure 9. Calculated results. (a) Band structure, (b) corresponding density of states, (c) crystalline structure (purple: Sb; orange: Te), and (d) dielectric functions for Sb_2Te in HEX geometry.

the *c* axis, as described in the previous section. Figures 9(a) and (b) shows the corresponding calculated band structure, partial, and total density of states (DOS). The band structure illustrates that Sb_2Te is a semimetal material. The valance band of ST film mainly consists of Sb and Te *p* states, and minor contributions from Sb *s* state. Therefore, the peaks of ε_2 in UV-vis region (figure 6(b)) corresponding to the strong optical absorption are associated with the Te *p* and Sb *p* state electronic transition. Furthermore, the bottom of the conduction band and the top of the valence band are consisted of Sb states coming from both the Sb_2Te_3 units and the Sb bilayers, which is in accordance with the previous study [6]. Based on the analysis of spectroscopic ellipsometry, ST film in amorphous structure is a semiconductor with an optical band gap of 0.39 eV. The transition from semiconductor to semimetal corresponds to the change from AM to HEX phase. The band gap narrowing phenomenon is similar with other chalcogenide phase change compounds [32, 40, 41].

The calculated and experimental dielectric functions of ST in HEX phase are shown in figure 9(d). To eliminate the unwanted temperature effects, the experimental data were extracted from the ellipsometric spectra as the temperature cooling down to 300 K from 620 K. Note that the ST material systems cannot restore them back to amorphous structure after slow heating [32]. In order to validate the theoretical solutions, the calculated dielectric functions were compared with the experimental results. The broad peaks of ε_2 for experimental and calculated data are located at about 1.5 and 1.7 eV, respectively. As a well-known problem of calculations based on density-functional theory (DFT), the calculated optical band gaps are underestimated by about 20–30%, as compared with the experimental values. It is reasonable that the calculated optical transition energies could be lower than the experimental results. In addition, the Drude peak in IR region is obtained successfully. Therefore, the calculated results are in good agreement with the experimental data. The present first-principles calculation method is reliable and can be used to make qualitative analysis in the materials with similar multilayered structures.

4. Conclusions

In summary, optical/electronic properties and microstructure variations of WST films as functions of temperature and W concentration have been systemically investigated by temperature dependent XRD, Raman scattering, and spectroscopic ellipsometry experiments. Based on the temperature properties of diffraction peaks, phonon modes, and dielectric functions, the intermediate crystalline state of ST and WST films between amorphous and HEX phases is presented, which is a mixture of crystalline Sb and Te. It provides an important insight on the physical mechanism of phase change system. The electronic band structure calculation shows that the ST in HEX phase is a semimetal. Based on the good agreement between experimental and calculated results, it can be concluded that the present first-principles calculation method can be used to make qualitative analysis in the materials with similar multilayered structures.

Acknowledgment

This work was financially supported by Major State Basic Research Development Program of China (Grant Nos. 2013CB922300 and 2011CB922200), Natural Science Foundation of China (Grant Nos. 11374097 and 61376129), Projects of Science and Technology Commission of Shanghai Municipality (Grant Nos. 15JC1401600, 14XD1401500, 13JC1402100 and 13JC1404200), and the Program for Professor of Special Appointment (Eastern Scholar) at Shanghai Institutions of Higher Learning.

References

[1] Kolobov A V, Fons P, Frenkel A I, Ankudinov A L, Tominaga J and Uruga T 2004 *Nat. Mater.* **3** 703
[2] Wuttig M and Yamada N 2007 *Nat. Mater.* **6** 824
[3] Lencer D, Salinga M, Grabowski B, Hickel T, Neugebauer J and Wuttig M 2008 *Nat. Mater.* **7** 972
[4] van Pieterson L, Lankhorst M H R, van Schijndel M, Kuiper A E T and Roosen J H J 2005 *J. Appl. Phys.* **97** 083520
[5] Youm M S, Kim Y T, Kim Y H and Sung M Y 2008 *Phys. Status Solidi a* **205** 1636
[6] Govaerts K, Sluiter M H F, Partoens B and Lamoen D 2012 *Phys. Rev.* B **85** 144114
[7] Peng C, Wu L C, Rao F, Song Z T, Yang P X, Song H J, Ren K, Zhou X L, Zhu M, Liu B and Chu J H 2012 *Appl. Phys. Lett.* **101** 122108

[8] Zhu M, Wu L C, Rao F, Song Z T, Li X L, Peng C, Zhou X L, Ren K, Yao D N and Feng S L 2011 *J. Alloys. Compd.* **509** 10105
[9] Rao F, Ren K, Gu Y F, Song Z T, Wu L C, Zhou X L, Liu B, Feng S L and Chen B 2011 *Thin Solid Films* **519** 5684
[10] Raoux S, Salinga M, Sweet J L J and Kellock A 2007 *J. Appl. Phys.* **101** 044909
[11] Lu Y G, Song S N, Song Z T, Rao F and Wu L C 2012 *Appl. Phys. Lett.* **100** 193114
[12] Perdew J P, Burke K and Ernzerhof M 1996 *Phys. Rev. Lett.* **77** 3865
[13] Klimes J, Bowler D R and Michaelides A 2011 *Phys. Rev.* B **83** 195131
[14] Monkhorst H J and Pack J D 1976 *Phys. Rev.* B **13** 5188
[15] Meng Y, Ji X L, Han P G, Song Z T, Zhou W Y, Guo W J, Qian B and Wu L C 2015 *ECS Solid State Lett.* **4** P4
[16] Guo S, Hu Z G, Ji X L, Huang T, Zhang X L, Wu L C, Song Z T and Chu J H 2014 *RSC Adv.* **4** 57218
[17] Mazzarello R, Caravati S, Angioletti-Uberti S, Bernasconi M and Parrinello M 2010 *Phys. Rev. Lett.* **104** 085503
[18] Nemec P, Nazabal V, Moreac A, Gutwirth J, Benes L and Frumar M 2012 *Mater. Chem. Phys.* **136** 935
[19] Sosso G C, Caravati S, Mazzarello R and Bernasconi M 2011 *Phys. Rev.* B **83** 13420
[20] Andrikopoulo K S, Yannopoulos S N, Voyiatzis G A, Kolobov A V, Ribes M and Tominaga J 2006 *J. Phys.: Condens. Matter* **18** 965–79
[21] Gilliam S J, Jensen J O, Banerjee A, Zeroka D, Kirkby S J and Merrow C N 2004 *Spectrochim. Acta* A **60** 425
[22] Zhang W, Ronneberger I, Li Y and Mazzarello R 2014 *Mon.hefte Chem.* **145** 97
[23] Agafonov V, Rodier N, Céolin R, Bellissent R, Bergman C and Gaspard J P 1991 *Acta Crystallogr.* C **47** 1141
[24] Sosso G C, Caravati S and Bernasconi M 2009 *J. Phys.: Condens. Matter* **21** 095410
[25] Pine A S and Dresselhaus G 1971 *Phys. Rev.* B **4** 356
[26] Russo V, Bailini A, Zambon M, Passoni M, Conti C, Casari C S, Li Bassi A and Bottani C E 2008 *J. Raman Spectrosc.* **39** 205
[27] Liang N T 1983 *Opt. Lett.* **8** 374
[28] Hunger R, Blick N, Esser N, Arens M, Richter W, Wagner V and Geurts J 1994 *Surf. Sci.* **307** 1061
[29] Zhang S, Zhang J Z, Han M J, Li Y W, Hu Z G and Chu J H 2014 *Appl. Phys. Lett.* **104** 041106
[30] Zhang J Z, Tong W Y, Zhu J J, Xu J Y, Duan Z H, Xu L P, Hu Z G, Duan C G, Meng X J, Zhu Z Q and Chu J H 2015 *Phys. Rev.* B **91** 085201
[31] Cho Y J, Nguyen N V, Richter C A, Ehrstein J R, Lee B H and Lee J C 2002 *Appl. Phys. Lett.* **80** 1249
[32] Guo S, Ding X J, Zhang J Z, Hu Z G, Ji X L, Wu L C, Song Z T and Chu J H 2015 *Appl. Phys. Lett.* **106** 052105
[33] Jellison G E Jr and Modine F A 1996 *Appl. Phys. Lett.* **69** 371
[34] Jellison G E Jr and Modine F A 1996 *Appl. Phys. Lett.* **69** 2137
[35] Shportko K, Kremers S, Woda M, Lencer D, Robertson J and Wuttig M 2008 *Nat. Mater.* **7** 653
[36] Seo Y K, Chung J-S, Lee Y S, Choi E J and Cheong B 2012 *Thin Solid Films* **520** 3458
[37] Mendoza-Galván A and González-Hernández J 2000 *J. Appl. Phys.* **87** 760
[38] Dejneka A, Aulika I, Trepakov V, Krepelka J, Jastrabik L, Hubicka Z and Lynnyk A 2009 *Opt. Express* **17** 14322
[39] Majidi M A *et al* 2013 *Phys. Rev.* B **87** 235135
[40] Orava J, Wágner T, Šik J, Přikryl J, Frumer M and Beneš L 2008 *J. Appl. Phys.* **104** 043523
[41] Park J-W, Eom S H and Lee H 2009 *Phys. Rev.* B **80** 115209